Panu, Hildén; Timo, Rajamaki; Thomas, Fordell; Makkonen, Jarkko; Alyshev, Sergei; Kharakhordin, Alexandr; Firstov, Sergei

Real-time HCl gas detection at parts-per-billion level concentrations utilising a diode laser and a bismuth-doped fibre amplifier

PAPER • OPEN ACCESS

Real-time HCl gas detection at parts-per-billion level concentrations utilising a diode laser and a bismuth-doped fibre amplifier

Real-time HCl gas detection at parts-per-billion level concentrations utilising a diode laser and a bismuth-doped fibre amplifier

Hildén Panu[1]**, Rajamäki Timo**[2] **, Fordell Thomas**[2]**, Jarkko Makkonen**[3]**, Sergei Alyshev**[4]**, Alexandr Kharakhordin**[4] **and Sergei Firstov**[4]

[1] Department of Applied Physics, Aalto University, Tietotie 3, FI-02150 Espoo, Finland
[2] VTT, National Metrology Institute VTT MIKES, Tekniikantie 1, FI-02150 Espoo, Finland
[3] Optoseven Oy, Tekniikantie 2, FI-02150 Espoo, Finland
[4] Prokhorov General Physics Institute of the Russian Academy of Sciences, Dianov Fiber Optics Research Center, 38 Vavilov, 119333 Moscow, Russia

E-mail: timo.rajamaki@vtt.fi

CrossMark

Abstract

HCl measurements in a cleanroom environment are carried out using a cavity ring-down analyser in order to get an estimate of the HCl concentrations that can be expected to be present in semiconductor manufacturing. HCl is a reactive gas and the materials used for gas sampling and transportation have a significant effect on the measurement response time; hence, data on HCl adsorption to different materials is also provided. Finally, a light source operating at 1742 nm that can be used for HCl detection in a multi-gas analyser based on multipass photo-acoustic spectroscopy is presented. Preliminary results indicate that sub-ppb detection levels are achievable using this approach even for HCl.

Keywords: gas sensing, photoacoustic spectroscopy, laser, bismuth, fibre, cleanroom

(Some figures may appear in colour only in the online journal)

1. Introduction

The presence of airborne molecular contaminants (AMCs) such as HCl, NH_3 and HF is a key factor affecting production yields in the cleanrooms of the semiconductor industry [1–3]. Real-time monitoring of variations in AMC concentrations during the manufacturing process would enable corrective actions to be taken, resulting in improved yields and cost savings [2, 3]. Moreover, the chemicals used can be of concern not only in regard to process contamination but in regard to occupational health and safety as well.

To this end, an optical instrument based on multipass photoacoustic spectroscopy (PAS) that enables simultaneous sensing of NH_3 and HF has been developed previously [4, 5]. The working principle of PAS has been discussed in detail by several authors (see, e.g. [6–8]). The developed spectrometer uses a cantilever microphone, which has been demonstrated to obtain high signal-to-noise ratios [9, 10]. In the present work, we add HCl to its measurement capabilities. The instrument operates in the near-infrared, sacrificing the sensitivity achievable with fundamental transitions in the mid-IR but taking advantage of the light sources and optics more readily available at overtone wavelengths in the near infrared.

Light from three independent, all-fibre master oscillator power amplifiers (MOPAs) is combined with

wavelength-division multiplexers (WDMs). Near-infrared beams from the seed lasers operating at 1527 nm and 1321 nm and used for NH_3 and HF detection are amplified using well-established erbium-doped fibre amplifiers (EDFAs) and semiconductor optical amplifiers (SOAs) respectively. In the case of the 1742 nm used for HCl, efficient rare-earth-doped fibre or semiconductor amplifiers are not available; however, in recent years bismuth-doped fibres (BDFs) that are capable of providing amplification in different spectral bands in the near-infrared, including the 1600–1800 nm range, have been demonstrated. The first BDFs with aluminosilicate glass cores were fabricated in 2005 [11]. Initially, the bismuth-doped fibre amplifiers (BDFAs) operated in the 1140–1225 nm range [12, 13]. Later, longer wavelengths were covered by BDFAs based on germanosilicate glass [14, 15] and phosphogermanosilicate glass [14, 16, 17]. Recently, amplification in the 1625–1775 nm band has been obtained using bismuth-doped high-germania-glass-core fiber [18], which was used to develop bismuth fibre lasers [19] and BDFAs [20]. Current research on BDFAs is principally focused on telecommunications applications, but BDFAs can also be useful for remote gas sensing at 1687 nm as shown very recently in [21]. To the best of the authors' knowledge, BDFAs applied to the detection of HCl at 1742 nm have not been presented yet.

This work is organised as follows. In the next section, HCl concentration measurements performed in a cleanroom manufacturing site using a commercial cavity ring-down analyser are presented. These measurements were made in order to get an estimate for the relevant HCl concentrations that can be expected to be present in a semiconductor manufacturing environment. The tests included measurements in close proximity to some of the most likely HCl contaminant sources in a cleanroom. In section 3, we present our measurements of the dependence of the gas transportation time on different sampling tube materials. These results can then be used to choose construction materials for the measurement system in order to optimise the response time in HCl sensing, which, along with sensitivity, is a crucial parameter for the real-time monitoring of reactive gases such as HCl, NH_3 and HF. Based on these investigations, in section 4 we provide details on the design and performance of the new MOPA laser source for HCl spectroscopy in the near-infrared and present an overview of the developed instrument. In section 5, the preliminary results for HCl detection using the developed photo-acoustic spectroscope are presented. Section 6 summarises the work and highlights the main results.

2. Cleanroom measurements

The goal of the cleanroom measurements was to get an idea of what kind of HCl concentrations can be expected in semiconductor manufacturing. HCl measurements were made at close proximity to the most likely HCl contaminant sources typically met within a cleanroom, which are the chemical containers, spray units, and wet benches (the chemical
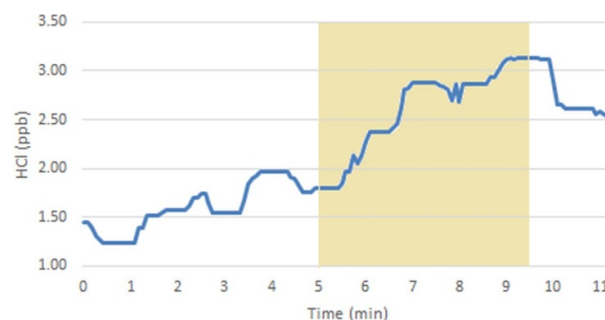

Figure 1. The measured HCl concentration from the chemical tank container after the HCl tank was briefly opened for a duration indicated by the yellow background.

process stations). Such measurements are important in order to see if these sources pose any real concern for fabrication yields or occupational safety. A commercial cavity ring-down spectrometer (CRDS; Tiger Optics i-2000) was used in these measurements and a polytetrafluoroethylene (PTFE; commonly named Teflon) sampling tube was used to gain proximity of potential contamination sources. The utilised CRDS model is specified to have a sensitivity of 0.75 ppb and a speed of response of 90% within <2 min.

2.1. Chemical containers

The first potential HCl source measured was a chemical container with an HCl tank inside. First, the sampling tube was placed next to an HCl tank container, and then it was moved inside. In neither case were any levels of concentration detected by the analyser; the reading remained at the 1–1.5 ppb background level. Next, the cover of the HCl tank inside the container was briefly opened. With the measuring end of the tube still located inside the container, a noticeable increase in the HCl occurred, as shown in figure 1. The increase in HCl concentration within the container, while clearly detectable, is only minor, which is due to the strong ventilation within the container. Finally, the HCl was measured during HCl tank replacement. During the replacement, the measurement tube was located next to a container with the head above the container. The measured HCl concentration increased significantly during the replacement, specifically when the replacement tank passed by the measuring head of the tube. The increase in HCl concentration is shown in figure 2. The figure shows a rapid rise in the concentration followed by a slow decrease. The slow decrease is due to HCl stuck inside the tube and analyser, and is not an indication of HCl being left to linger in the cleanroom air. After the HCl tank replacement, the HF tanks within the same container unit were also replaced. During the HF tank replacement, we tried to see if the interaction with HF would affect the measured HCl concentration, but such an affect was not detected.

While the chemical tank exchange significantly elevated the airborne HCl levels, the levels were still well below the indicative occupational exposure limits for EU member states:
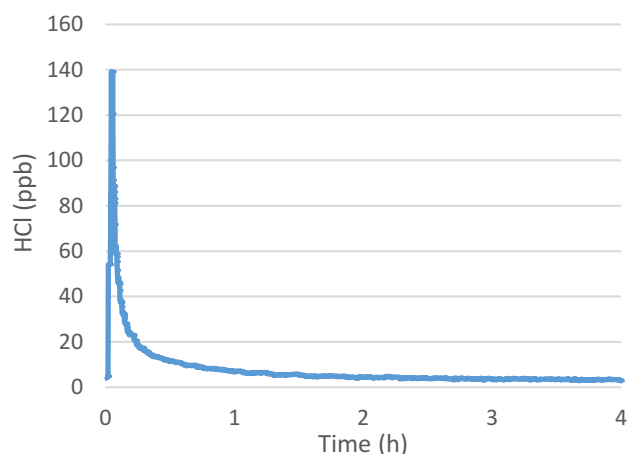
Figure 2. The measured HCl concentration outside the chemical tank container during and after HCl tank replacement. The measured concentration remains elevated for a long time due to the desorption of HCl left inside the tube and analyser.

5 ppm by air volume for a time-weighted average 8 h and 10 ppm at all times [22].

2.2. The spray unit

A spray unit can be used for etching, cleaning and resist stripping by spraying chemicals onto the wafers. Initially, the sampling tube was placed next to the chemical (HCl, HF and NH_3) input contacts of the process chamber, where the chemicals are first diluted and then sprayed onto the wafers placed within the unit. While in the unit, a process cycle was run. The cycle took approximately 45 min to complete and it included wafer cleaning using HCl, HF and NH_3; rinsing using O_3 and H_3O; and drying with NH_3O. During the process, no significant deviation from ambient conditions was detected and the HCl concentration stayed constant at the 0.6 ppb background level.

2.3. The wet bench

The last HCl source studied was a wet bench with an HCl solution bath. The process solution is a concentrated mixture of HCl and H_3O H_3O. Such mixtures are typically used for removing metals such as Fe, Ni and, especially, Cu, which cannot be removed using an HF solution (which is needed for removing Al). First the bath cover was opened and the HCl concentration was measured from the top of the bench, as shown in figure 3(a). The sampling tube was left there for a couple of minutes during which time nothing notable was measured. Afterwards, the sampling tube was put at the front side of the bench, approximately 50 cm below the top (as shown in figure 3(b)) and the tube head was left next to the wet bench for the whole working day. People operating the wet bench were not notified of the ongoing measurement in order that the wet bench would be operated as it naturally would be. In this way, the human factor of wet bench operation could also be taken into account. While the tube head was left to measure, two spikes with different HCl concentrations were
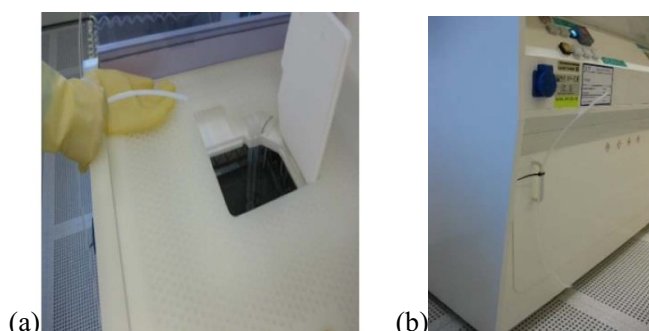

Figure 3. (a) Measurement of HCl next to an open HCl bath; (b) the wet bench with an HCl solution bath above the measurement tube head.
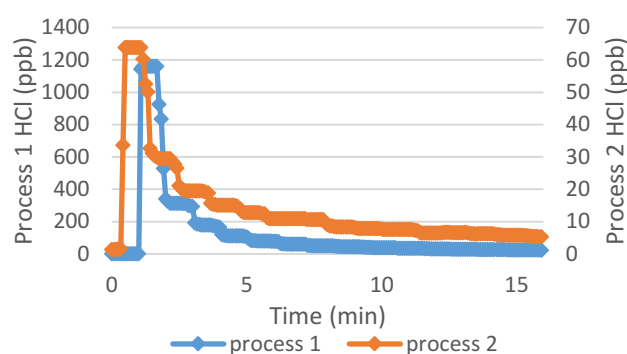

Figure 4. Detected HCl concentration spikes next to the wet bench with an HCl bath during and after use of the bath.

detected (shown in figure 4). This shows how great an impact the individual operating the wet bench can have on preventing contamination.

3. Material tests

In addition to high sensitivity, the sensing of AMCs for semiconductor manufacturing demands fast response times. When the goal is to measure highly reactive molecules—such as HCl, NH_3 and HF—the material of the tubes used for the transportation of a gas sample to an analyser and other system inner parts that are in contact with the sample gas should be chosen carefully. These materials significantly affect the gas transportation time due to adsorption to their surfaces. This can be the main factor determining the response time of a setup, as was shown for NH_3 [23, 24]. In addition, the use of an inappropriate tube material may lead to enhanced interaction between the gas molecules and the tube surface, accelerating the degradation of the analyser. We performed a series of measurements of gas mixtures with a high HCl concentration when the transportation of the tested gas was provided by tubes with different chemical compositions. In particular, three of the tested tubes were made of fluoropolymers: perfluoroalkoxy alkane (PFA), PTFE and polyvinylidene difluoride (PVDF). The other tubes were stainless steel tubes: one with a bright finish called SS that has an unspecified arithmetic mean roughness (Ra), a sample of Ultron-SS with (Ra < 0.25 μm) and a tested sample

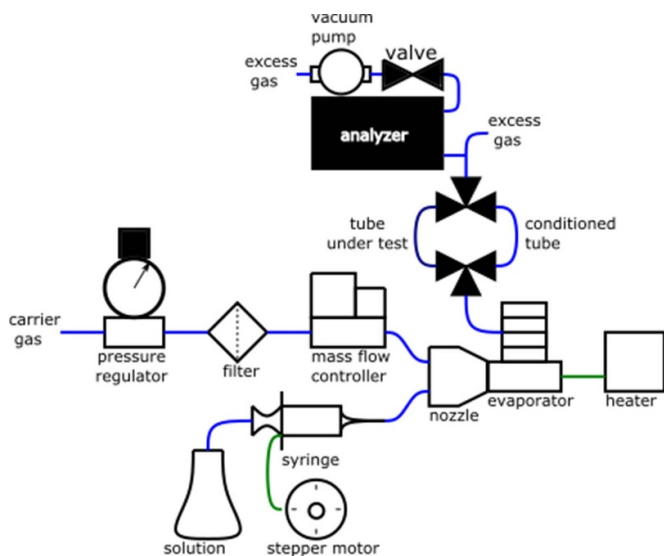**Figure 5.** A schematic of the setup used to measure the adsorption of HCl molecules for various tubes.

Figure 6. A dynamic of the HCl molecule concentration changes induced by adsorption to a surface of a 9.44 m long PVDF tube.

Table 1. The measured response times and the number of adsorbed molecules per square centimetre of tube surface for different tubes.

Tube	Length (m)	t_{90} (s)	N (molecules cm^{-2})
PTFE	10	531	4.9×10^{11}
PVDF	9.44	1252	1.5×10^{13}
PFA	10	927	2.8×10^{12}
Silconert	5	341	3.3×10^{11}
Ultron	1	922	2.0×10^{13}
SS	1	2304	9.4×10^{13}

with an amorphous silicon coating (Silconert 2000). All of the tested tubes had outer and inner diameters of 6 and 4 mm respectively.

Figure 5 depicts the experimental setup. The HCl containing gas mixtures are generated using the gas generator included. In order to obtain the required gas mixture, a solution containing a certain HCl concentration was initially prepared and then inserted into the gas generator. Thereafter, this solution was fed by syringe into an evaporator at the rate of 0.07 g min^{-1}, controlled by a stepper motor system. In addition to the solution, the gas generator takes in pressurised air that works as a carrier gas and passes it through a pressure regulator, a filter and a mass flow controller that were used to obtain the desired parameters. To obtain the correct concentration of HCl in the reference gas sample, all the parameters were controlled with a home-made LabVIEW application. The solution and the carrier gas were guided to a nozzle, which sprayed the gas and the solution onto the evaporator, generating the gas mixture. The gas generator was developed by Optoseven Ltd together with VTT Ltd. A detailed description of its operation can be found in [25].

The tubing between the generator and analyser consists of two tubes placed in parallel. One of them is the tube under test and the other tube (the conditioning tube) is used to keep the gas running between measurements. This ensures that, at the beginning of a measurement, all surfaces besides the tested tube are conditioned, that is, the HCl adsorption and desorption processes occur at the same rates. Two three-way valves are used to control the gas path from the generator to the analyser, which is the same CRDS that was used in the field tests.

The setup is ready for the measurements when it is conditioned and the tube under test is connected to the generator and the analyser with the valves closed. The measurement starts by opening the valves that redirect the gas flow through the
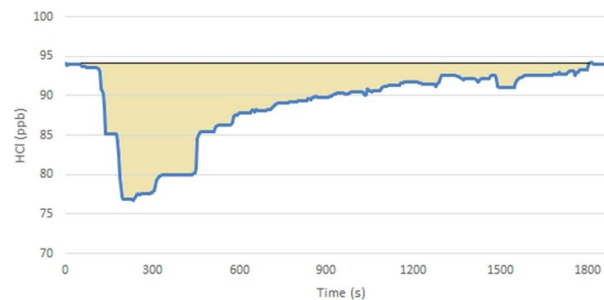
tube under test. This results in a decrease in HCl concentration in the analyser due to the adsorption of HCl molecules to the tube surface. The HCl concentration is measured until the tube under test is conditioned. Thereafter, the valves are turned again to guide the gas through the conditioning tube, while the next measurement is prepared.

An example of a measurement time series is shown in figure 6. A rapid decrease in HCl concentration takes place when the gas was fed to the tube under test. Shortly after this, the HCl concentration begins to increase until the tube is conditioned, and the concentration reaches the original value.

In addition to the response time t_{90}, which, according to ISO 26142 [26], is the time taken for an analyser to reach 90% of the final indication, the graph shown in figure can be used to calculate the number of molecules adsorbed, which corresponds to the area highlighted in yellow. The measured response times and the number of adsorbed molecules (*N*) for a 100 ppb HCl (and 1.1% H_2O) containing gas sample for different tubes are presented in table 1. It should be noted that we used longer tubes for materials with good response times, since otherwise the decrease in concentration would be small. Additionally, the conditioning of long tubes made out of poor materials would take unpractically long. The use of different tube lengths affects the response time but not the adsorption (molecules/area). We can conclude that the tubes made of PTFE and Silconert were preferred since they have the lowest response times and lowest number of adsorbed molecules per unit area.
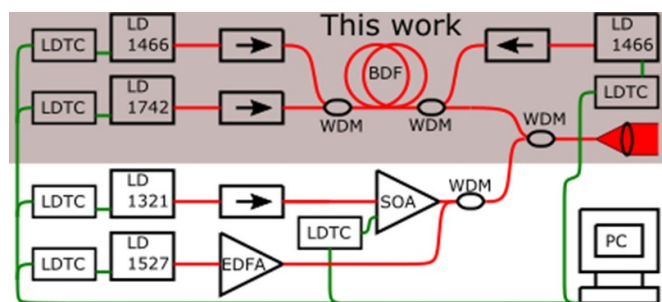
Figure 7. A schematic of the MOPA-based fibre laser system for the photoacoustic sensing of HCl (1742 nm), HF (1321 nm) and NH$_3$ (1527 nm).

4. MOPA light sources for HCl, NH$_3$ and HF

HCl is not the only problematic AMC present in a cleanroom environment. Therefore, effective AMC monitoring using commercially available spectroscopic analysers often requires a number of analysers, usually one for each AMC of interest. In earlier work, a sensitive analyser based on multi-pass PAS and capable of measuring HF and NH$_3$ simultaneously was developed [4, 5]. The absorption processes corresponding to the different molecules were set to generate acoustic signals at distinct frequencies by using different modulation frequencies for the laser diodes (LDs). The acoustic signals at different frequencies can be measured and processed simultaneously with ease. The instrument's lowest detection limit was 5 ppb for NH$_3$ and 0.5 ppb for HF [4].

Since the sensitivity of PAS scales linearly with power, the challenge is to develop a laser system capable of illuminating a sample at multiple wavelengths with sufficient power simultaneously. A schematic of the laser system is shown in figure 7. Fiber-coupled LDs operating at 1321 nm, 1527 nm and 1742 nm were used as seed sources for the amplifiers: a 100 mW O-band SOA (Thorlabs BOA-1132) and a C-band 500 mW EDFA (HLOA-F5127). Fused WDMs were used to combine the signals to the PAS. In the following sub-sections, details on the design and performance of the 1742 nm light source will be given.

4.1. A MOPA laser based on a BDFA

The seed laser is a 5 mW distributed-feedback semiconductor laser with a 2 MHz linewidth and a 40 dB side-mode suppression ratio. It can be thermally tuned to the strongest absorption line of HCl in the near infrared at 1742.38 nm (5739.26 cm^{-1}). Figure 8 shows the main absorption lines of HCl, H$_2$O and CH$_4$, located near the absorption line of interest. In figure 8, the absorption strength (line height) is given for equal number of molecules, whereas figure 9 shows a simulated spectrum for an example gas mixture containing 100 ppb HCl, 1.1% H$_2$O and 1 ppm CH$_4$ at the temperature of 300 K and at atmospheric pressure. This illustrates the relative weakness of absorption for trace amounts of HCl with respect to typical H$_2$O absorption and, accordingly, the potential interference of H$_2$O in the HCl reading.
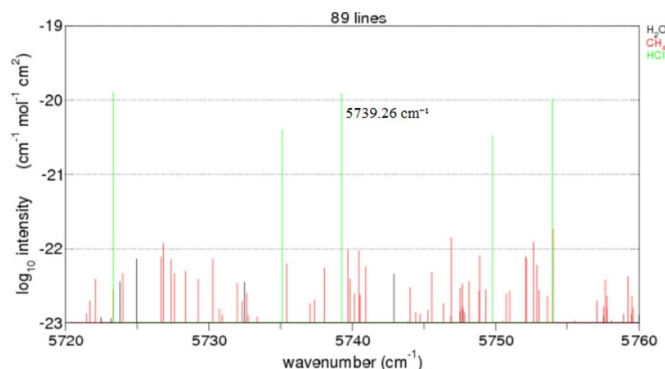

Figure 8. The absorption spectra of HCl (green), H$_2$O (black) and CH$_4$ (red) gases derived from the HITRAN (2016) database.
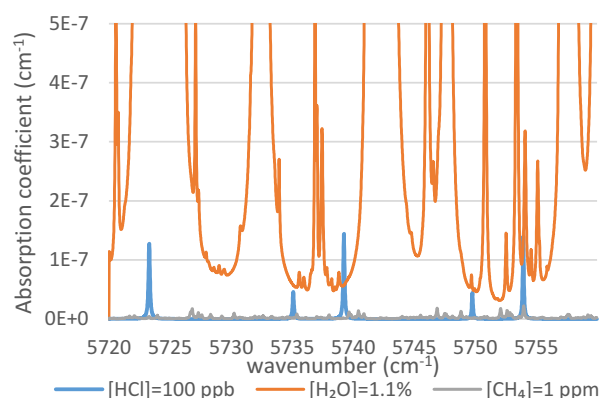

Figure 9. The simulated absorption spectra of a gas contain 100 ppb HCl (blue), 1.1% H$_2$O (orange) and 1 ppm CH$_4$ (grey) using the SpectraPlot simulation tool and HITRAN (2012) data at the temperature of 300 K and at atmospheric pressure.

4.1.1. BDF. The Bi-doped high-GeO$_2$–SiO$_2$ fibre used in the BDFA is a promising active medium for different optical devices—such as optical amplifiers, continuous wave and pulsed lasers—operating in the 1600–1800 nm range. A BDF preform was fabricated using the modified chemical vapour deposition technique. The refractive index difference between the core and cladding of the preform, measured by a Photon Kinetics 2600 profiler, was 0.07, giving a numerical aperture of ∼0.45. A single-mode BDF, with the outer and core diameters of 2.2 μm and 125 μm respectively, was drawn from this preform at a speed of 10 m min^{-1} at a temperature of 1900 °C. The second-mode cut-off wavelength of the BDF was 1.4 μm. The parameters of the used BDF differ considerably from that of conventional fibres (similar to SMF-28), which leads to a significant splice loss of about 1 dB.

The laser transitions in BDFs are attributed to the bismuth-related active centres having a wide absorption band which peaks at 1.63 μm with a width of ∼150 nm [19, 20, 27, 28]. Commonly, the pump wavelength is chosen so that it falls into the short-wavelength edge of this absorption band. In this case, one can see the intensive emission with a peak near 1.73 μm. Detailed information on the absorption and
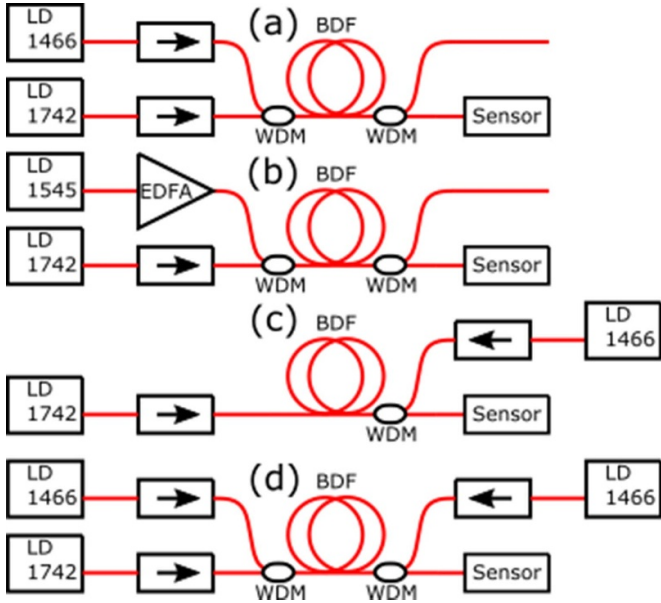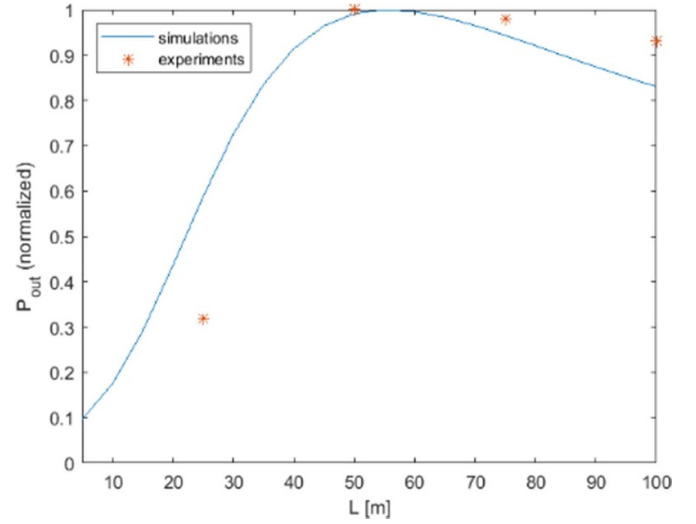
Figure 11. Normalised output power as a function of the BDF length of a BDFA with bi-directional pumping configuration.

Figure 10. The configurations of the BDFA at 1742 nm pumped 1466 or 1545 nm for the MOPA laser system. In parts (a) and (b) the additional WDM at the output was used for elimination of the unabsorbed pump power.

luminescent properties of the active centres, including the energy level configurations, can be found in [19, 28].

It should be noted that BDF is characterised by the low absorption of $\sim$2 dB m^{-1} at $\lambda = 1.63$ μm due to the small Bi concentration (<0.1 mol %); however, even with such a low Bi content, the unsaturable loss is $\sim$0.1–0.2 dB m^{-1} for all the studied regions, which is critical for the development of the devices. The small-signal gain coefficient of the BDF was experimentally obtained to be 0.5–0.7 dB m^{-1} for 1532 nm pumping.

4.1.2. BDFA characterisation (simulation and experiments).
The optimisation of the BDFA design includes the search for the optimal pump wavelength, the length of the active fibre and testing different pumping configurations. The series of BDFA configurations presented in figures 10(a)–(d) was studied experimentally.

A numerical simulation of the BDFA was carried out using a standard approach, where a set of equations that can be presented in the form [29, 30]

$$\pm \frac{\partial}{\partial z} P(\omega_i, z)^{\pm} = \Big[g_{21} \left(\omega_i, z; P(\omega_1, z)^{\pm}, \ldots, P(\omega_\kappa, z)^{\pm} \right)$$
$$- g_{12} \left(\omega_i, z; P(\omega_1, z)^{\pm}, \ldots, P(\omega_\kappa, z)^{\pm} \right) \Big]$$
$$\times P(\omega_i, z)^{\pm} + 2 g_{21} \left(\omega_i, z; P(\omega_1, z)^{\pm}, \ldots, \right.$$
$$\left. \times P(\omega_\kappa, z)^{\pm} \right) P_0 (\omega_i) - \alpha P(\omega_i, z)^{\pm}$$

was solved. The calculation was performed using a finite difference method where the full spectral band is divided into a finite number of spectral components with angular frequencies from ω_1 to ω_κ. The power of the spectral component is $P^{\pm} (\omega_i)$,

with $\omega = \omega_i$ for the forward (+) and backward (−) propagating beams. Each differential equation describes the evolution of the power of the corresponding spectral component along the active fibre taking into account the stimulated emission ($g_{21}P$), absorption ($g_{12}P$), amplified spontaneous emission ($2g_{21}P_0$), and attenuation (αP) caused by the background loss (unsaturable loss) and insertion losses. Here, P_0 denotes the power of spontaneous optical noise, α is the attenuation coefficient, and g_{21} and g_{12} are the laser-level population-dependent coefficients related to the stimulated emission and ground state absorption respectively. The set of equations is solved numerically for a variety of boundary conditions, which are determined by the power and wavelength of the lasers used to illuminate the BDF. More details on the simulation can be found in [31].

Pumping at 1545 nm (figure 10(b)) is more efficient compared to pumping at 1466 nm (figure 10(a)); the former is measured (simulated) to yield the same output power as the latter but with 31% (simulated 37%) less pump power. Nevertheless, we chose to proceed with the simpler option of pumping the BDF with readily available and fairly powerful pump lasers at 1466 nm.

Figure 11 shows the normalised output power at 1742 nm, derived from the BDFA simulation as a function of the BDF length for the bi-directional pumping configuration (the configuration in figure 10(d)). The experimental data indicated by stars is presented for comparison. It can be seen that the results of the numerical calculations qualitatively coincide with the experimental results. The observable discrepancies are at least partly explained by the large uncertainties in the parameter values used in the simulation and presented in table 2. The simulation and the experiments both indicate that the optimum BDF length is about 50 m.

Figure 12 shows the output powers for different pumping configurations (see figure 10, parts (a), (c) and (d)) for both simulations and experiments for pump powers 50–400 mW. In this case, the length of the BDF was 50 m and the seed laser

Table 2. The parameters used for simulation of BDFA.

| Parameter	Definition	Value
N_{BAC}	BAC concentration	$\sim 10^{17}$
NA	Numerical aperture	0.45
α	Attenuation coefficient	0.15 dB m^{-1}
r_{core}	Core radius	1 μm
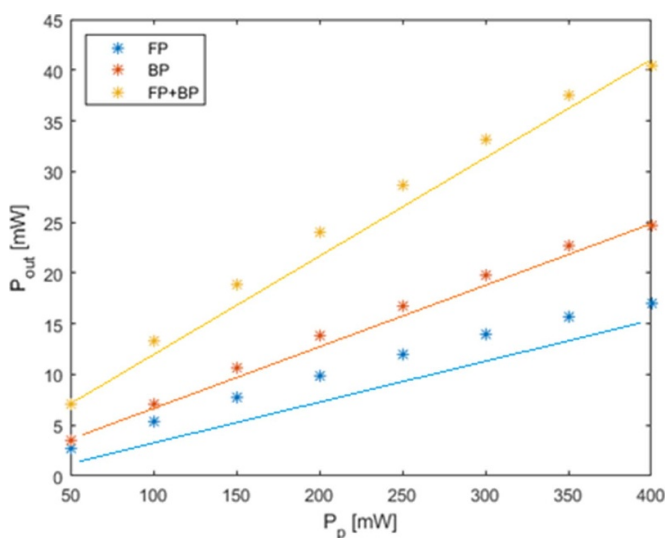
Figure 12. The output power after the BDFA (for different pumping schemes) based on a 50 m long BDF as a function of the pump power (the lines show the simulation, the stars show the experiment). In the bi-directional pumping configuration, both the pump lasers were used.

power was 5 mW. The results obtained are in good agreement for backward and bi-directional pumping schemes, and somewhat worse for the forward pumping configuration. These results indicate the consistency of the constructed model and the optimal design of the BDFA that was used for the MOPA laser system. The highest output power was obtained in the bi-directional pumping configuration with a total pump power of 800 mW. It is worth noting that in the test configurations, the fibre components were not spliced, and instead, connectors were used that introduced additional losses. The output power of the bi-directional configuration increased to 60 mW after splicing the fibre ends.

5. HCl gas detection experiments

The principle of a PAS is the photoacoustic effect, where the energy of a light beam absorbed by a gas target is converted, via collision-induced non-radiative transitions, into heat. Modulating the power of the light leads to a pressure wave that can be detected with high sensitivity. The signal measured by a PAS is proportional to the power of the laser radiation falling onto the studied sample; thus, in the absence of saturation, the sensitivity of a PAS can be increased by increasing the power of the laser.

Here, a GASERA PA201 analyser with a gas cell equipped with a cantilever microphone was used. A Herriot-type
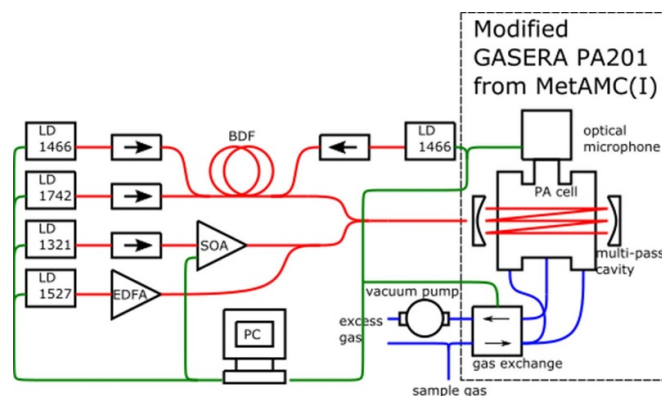
Figure 13. A diagram of the PAS analyser. The analyser has three LDs integrated into one laser source using WDMs. The laser source illuminates the multi-pass cavity of a photoacoustic cell based on a GASERA PA201 that was modified by VTT in the EMRP IND63 MetAMC project for airborne molecular contamination in manufacturing environments.
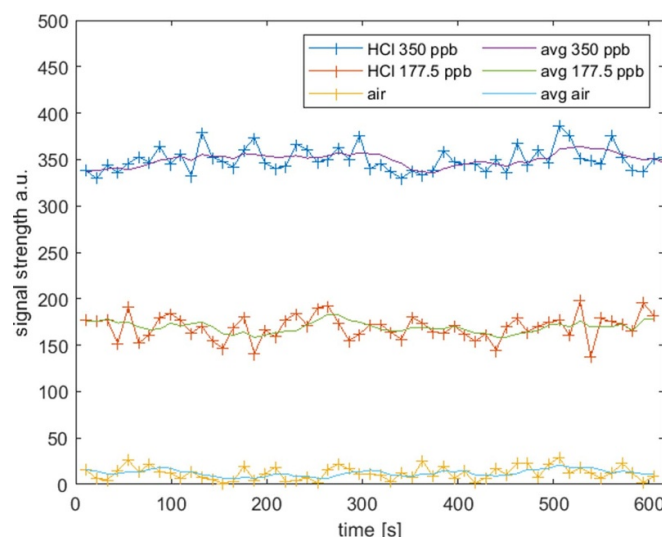
Figure 14. The temporal evolution of the signal strength of the gas mixtures with different HCl concentrations measured by the PAS analyser. Additionally, a similar trace for HCl-free compressed air is presented.

multi-pass cavity has been built around the cell in order to increase the interaction length and enhance the sensitivity (see figure 13). An integrated gas-exchange system can be used to change the gas sample periodically in the cell.

The optimised duration of a single measurement was 11 s, including 3 s for the gas exchange, 4 s for the cantilever relaxation after the gas exchange and 3.8 s for the measurement of the photoacoustic effect. Figure 14 shows an example of 10 min traces of the photoacoustic signal for two different HCl concentrations as well as pressurised air. Here, the optical power used was 53 mW. The signal strength of the analyser was calibrated with the 350 ppb HCl reference gas. The mean signal strengths for the measured data are shown in table 3.

Data like this can be used to determine the linearity, the limit of detection (LOD) and the measurement uncertainty of

Table 3. The mean signal strengths (μ) of the PAS analyser, calculated using the experimental data for gaseous mixtures with different HCl concentrations (C).

Sample	Air	HCl	
C (ppb)	—	177.5	350
μ	12	167.5	350
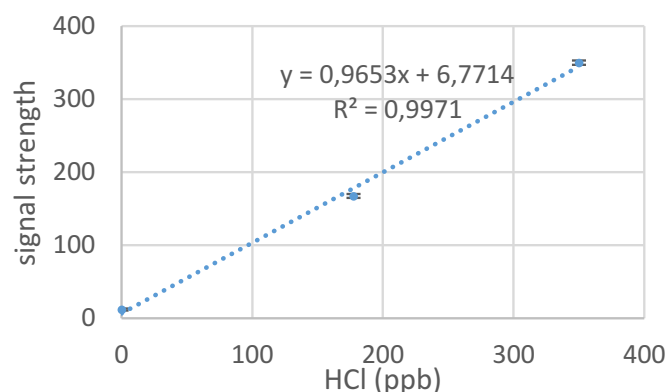
Figure 15. The mean values of the signal strengths measured from gases with [HCl] = 350 ppb, [HCl] = 177.5 ppb and compressed pure air (circles). The dotted line shows the linear function fit, and the error bars show the LOD values corresponding to the shortest averaging time of 3.8 s.

the analyser. For the LOD we used the following definition [32]:LOD $> 3\sigma/S$, where σ is the standard deviation of the noise of the instrument and S is the analytical sensitivity, which is a constant of proportionality between the generated signal strength and HCl concentration. Figure 15 shows the mean values of the signal strengths shown in figure 14. Generally, linearity is the relative deviation of an experimentally determined calibration graph from an ideal straight line. It can be seen that our experimental data can be fitted with a linear function with $R^2 > 0.99$. This confirms that the PAS analyser has a linear response in the measured concentration range. Analysing the data obtained for the compressed air, we established that the PAS analyser is capable of providing the correct measurements of the HCl concentration above 12 + LOD (ppb), where the LOD depends on the averaging time.

To determine the stability of the instrument, an Allan deviation was computed, which is used to investigate drifts and establish the sensor signal averaging limits [33]. The Allan deviation plot as a function of integration time is shown in figure 16 for an HCl concentration of 350 ppb. In this case the Allan deviation has a $1/\tau$ dependence (τ is the integration time) whereas $1/\sqrt{\tau}$ is more typical for spectroscopic analysers. Using the measured standard deviation $\sigma(3.8\text{ s}) = 15.55$ ppb and the Allan deviation, we can find a function that gives the LOD as a function of the integration time:

$$\text{LOD}(\tau) = \frac{3\sigma(\tau)}{S} \sim \frac{3\sigma(3.8\text{ s})\,3.8\text{ s}/\tau}{S}.$$
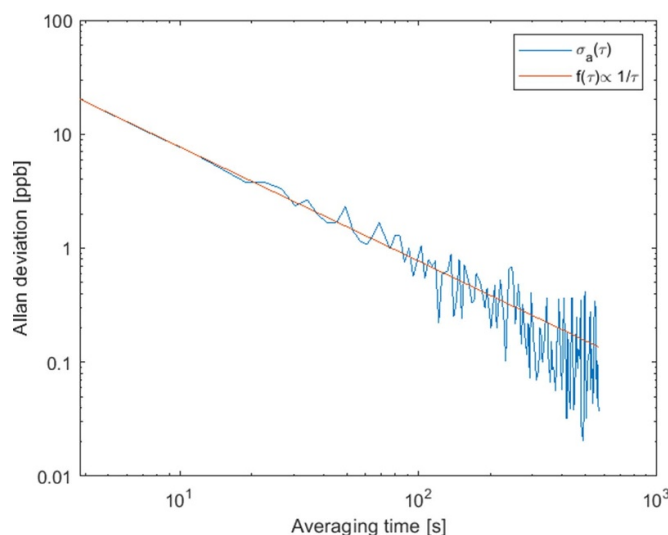
Figure 16. Allan deviation as a function of the integration time.

Table 4. LOD and standard deviation for the integration times of 3.8 s, 60 s and 300 s.

τ (s)	LOD (ppb)	σ (ppb)
3.8	48.31	15.55
60	3.06	0.98
300	0.61	0.20

The analytical sensitivity is $S \approx 0.97$, determined as the slope coefficient derived from the linear function fitting illustrated in figure 15. Using this, we can calculate the LOD for different integration times as listed in table 4.

As can be seen in table 4, when the integration time reaches 300 s, changes in the HCl concentration lower than 1 ppb can be detected. It should be underlined that the integration time of 300 s only includes the time taken by the analyser to record the signal without the other time intervals, in particular the time needed for gas exchange and cantilever relaxation. If the gas exchange is performed once in 300 s and the rest of time is spent for the measurements, the response time is poor. On the other hand, when a gas exchange is repeatedly performed (every 11 s, as was the case of the data in figure 14), the portion of time spent measuring the photoacoustic signal is reduced.

6. Conclusions

In summary, field tests on airborne HCl monitoring in a cleanroom environment were carried out, especially in proximity to HCl sources. We found that the measured HCl concentrations were too low for any health and safety concerns even when taken close to HCl sources. The baseline for the HCl concentration was below 0.5 ppb, which is hard to reach even for state-of-the-art analysers and leaves room for improvement considering the most stringent yield enhancement purposes. Fast analyser response times and fast recovery from concentrations that may be several orders of magnitudes above the

baseline are essential features for an analyser in clean room manufacturing environments.

In addition to the field tests, measurements of HCl adsorption to the surfaces of different sampling tube materials were carried out. Out of the six materials tested, PTFE, PFA, and Silconert adsorbed the least HCl molecules and these are therefore the materials that are best suited for tubes and surfaces that HCl comes into contact with.

Finally, following these guidelines we presented a novel instrument consisting of near-infrared laser light sources and multi-pass PAS for the simultaneous detection and monitoring of HF, NH_3 and HCl gases with a single analyser. For the first time, an optical amplifier based on a BDF was successfully used in the photoacoustic detection of HCl gas. These first results indicate that sub-ppb resolution can be achieved. However, the long measurement cycle with separate time slots for gas exchange, cell stabilisation and actual measurements hamper the use of this method with respect to measurement with absorption based techniques (e.g. CRDS).

Acknowledgments

ORCID iD

Rajamäki Timo https://orcid.org/0000-0002-0344-8850

References

[1] Franssila S 2010 *Introduction to Microfabrication* (New York: Wiley)

[2] EURAMET 2018 Publishable summary for 17IND09 MetAMCII metrology for airborne molecular contaminants II (www.euramet.org/research-innovation/search-research-projects/details/?tx_eurametctcp_project%5Bproject%5D=1536)

[3] ITRS 2015 International technology roadmap for semiconductors 2.0 (www.semiconductors.org/resources/2015-international-technology-roadmap-for-semiconductors-itrs/)

[4] EURAMET 2017 Final publishable JRP report for IND63 MetAMC metrology for airborne molecular contamination in manufacturing environments (www.euramet.org/research-innovation/search-research-projects/details/project/metrology-for-airborne-molecular-contamination-in-manufacturing-environments/)

[5] EURAMET 2016 Final publishable JRP summary for IND63 MetAMC metrology for airborne molecular contamination in manufacturing environments (www.euramet.org/research-innovation/search-research-projects/details/project/metrology-for-airborne-molecular-contamination-in-manufacturing-environments/)

[6] West G, Barret J, Siebert D and Reddy K 1983 Photoacoustic spectroscopy *Rev. Sci. Instrum.* **54** 797–817

[7] Frans J, Gina C, Jos O and Sacco L 2000 *Photoacoustic Spectroscopy in Trace Gas Monitoring* (New York: Wiley)

[8] Dumitras D, Dutu D, Matei C, Magureanu A, Petrus M and Popa C 2007 Laser photoacoustic spectroscopy: principles, instrumentation, and characterization *J. Optoelectron. Adv. Mater.* **9** 3655–701

[9] Kauppinen J, Wilcken K, Kauppinen I and Koskinen V 2004 High sensitivity in gas analysis with photoacoustic detection *Microchem. J.* **76** 151–9

[10] Koskinen V, Fonsen J, Kauppinen J and Kauppinen I 2006 Extremely sensitive trace gas analysis with modern photoacoustic spectroscopy *Vib. Spectrosc.* **23** 239–42

[11] Dvoyrin V, Mashinsky V, Dianov E, Umnikov A, Yashkov M and Guryanov A 2005 Absorption, fluorescence and optical amplification in MCVD bismuth-doped silica glass optical fibres *Proc. 31st European Conf. on Optical Communication, Technical Digest IEEE* paper Th 3.3.5

[12] Dianov E, Dvoyrin V, Mashinsky V, Umnikov A, Yashkov M and Guryanov A 2005 CW bismuth fibre laser *Quantum Electron.* **35** 1083–4

[13] Dianov E, Shubin A, Melkumov M, Medvedkov O and Bufetov I 2007 High power CW bismuth-fiber lasers *J. Opt. Soc. Am. B* **24** 1749–55

[14] Dianov E, Firstov S, Khopin V, Medvedkov O, Guryanov A and Bufetov I 2009 Bi-doped fibre lasers operating in the range 1470–1550 nm *Quantum Electron.* **39** 299–301

[15] Shubin A, Bufetov I, Melkumov M, Firstov S, Medvedkov O, Khopin V, Guryanov A and Dianov E 2012 Bismuth-doped silica-based fiber lasers operating between 1389 and 1538 nm with output power of up to 22 W *Opt. Lett.* **37** 2589–91

[16] Melkumov M, Bufetov I, Shubin A, Firstov S, Khopin V, Guryanov A and Dianov E 2011 Laser diode pumped bismuth-doped optical fiber amplifier for 1430 nm band *Opt. Lett.* **36** 2408–10

[17] Gumenyuk R, Puustinen J, Shubin A, Bufetov I, Dianov E and Okhotnikov O 2013 1.32 μm mode-locked bismuth-doped fiber laser operating in anomalous and normal dispersion regimes *Opt. Lett.* **38** 4005–7

[18] Firstov S, Alyshev S, Melkumov M, Riumkin K, Shubin A and Dianov E 2014 Bismuth-doped optical fibres and fiber lasers for a spectral region of 1600–1800 nm *Opt. Lett.* **39** 6927–30

[19] Firstov S, Alyshev S, Riumkin K, Melkumov M, Medvedkov O and Dianov E 2015 Watt-level, continuous-wave bismuth-doped all-fiber laser operating at 1.7 μm *Opt. Lett.* **40** 4360–3

[20] Firstov S, Alyshev S, Riumkin K, Khopin V, Guryanov A, Melkumov M and Dianov E 2016 A 23 dB bismuth-doped optical fiber amplifier for a 1700 nm band *Sci. Rep.* **6** 28939

[21] Gomolka G, Khegai A, Alyshev S, Lobanov A, Firstov S and Nikodem M 2020 Characterization of a single-frequency bismuth-doped fiber power amplifier with a continuous wave and modulated seed source at 1687 nm *Appl. Opt.* **59** 1558–63

[22] 2000 Commission directive 2000/39/EC of 8 June 2000 establishing a first list of indicative occupational exposure limit values in implementation of council directive 98/24/EC on the protection of the health and safety of workers from the risks related to chemical agents at work

Off. J. Eur. Communities L **142** 47 (https://eur-lex.
europa.eu/legal-content/EN/TXT/PDF/?uri=CELEX:
32000L0039&from=en)

[23] Vaittinen O, Metsälä M, Persijn S, Vainio M and Halonen L
2014 Adsorption of ammonia on treated stainless steel and
polymer surfaces *Appl. Phys.* B **115** 185

[24] Vaittinen O, Metsälä M, Halonen L, Persijn S, Leuenberger D
and Niederhauser B 2018 Effect of moisture on the
adsorption of ammonia *Appl. Phys.* B **124** 189

[25] Saxholm S, Rajamäki T, Hämäläinen J and Hildén P 2019
Dynamic calibration method for reactive gases *Meas. Sci.
Technol.* **31** 34001

[26] ISO 26142:2010 2010 Hydrogen detection
apparatus—stationary applications

[27] Firstov S, Alyshev S, Khopin V, Melkumov M, Guryanov A
and Dianov E 2015 Photobleaching effect in bismuth-doped
germanosilicate fibers *Opt. Express* **23** 19226–33

[28] Firstov S, Khopin V, Bufetov I, Alyshev S, Firstova E,
Guryanov A and Dianov E 2011 Combined
excitation-emission spectroscopy of bismuth active centers
in optical fibers *Opt. Express* **19** 19551–61

[29] Agrawal G 2004 *Lightwave Technology* (New York: Wiley)

[30] Desurvire E 1994 *Erbium-Doped Fiber Amplifiers* (New York:
Wiley)

[31] Hildén P 2019 Laser light source for photoacoustic
spectroscopy of hydrogen chloride *Master´s Thesis* (Aalto
University)

[32] Analytical Methods Committee 1987 Recommendations for
the definition, estimation and use of the detection limit
Analyst **112** 199–204

[33] Giglio M, Patimisco P, Sampaolo A, Scamarcio G, Tittel F and
Spagnolo V 2016 Allan deviation plot as a tool for
quartz-enhanced photoacoustic sensors noise analysis *IEEE
Trans. Ultrason. Ferroelectr. Freq. Control* **63** 555–60